Editors' Suggestion

Improvement of Write Efficiency in Voltage-Controlled Spintronic Memory by development of a Ta-B Spin Hall Electrode

Y. Kato,[*] Y. Saito,[†] H. Yoda, T. Inokuchi, S. Shirotori, N. Shimomura, S. Oikawa, A. Tiwari,
M. Ishikawa, M. Shimizu, B. Altansargai, H. Sugiyama, K. Koi, Y. Ohsawa, and A. Kurobe

Corporate R&D Center, Toshiba Corporation, Kawasaki 212-8582, Japan

Improving the write efficiency of magnetic tunnel junctions (MTJs) by using spin-orbit torque (SOT) is essential for realizing high-density spintronic memory. Here, we investigate a voltage-controlled spintronic memory (VoCSM) with a Ta-B spin Hall electrode. The magnetic properties of MTJs with a storage layer such as Fe-B or Co-Fe-B on an amorphous boride spin Hall electrode are found to exhibit an extremely small magnetic dead layer, a small saturation magnetization, and a large magnetic anisotropy. The spin Hall angle estimated by spin Hall magnetoresistance is -0.18 for the amorphous Ta-B spin Hall electrode, which is a magnitude twice that for a Ta spin Hall electrode. The write current density using SOT from the Ta-B spin Hall electrode is small compared with that from the β-Ta spin Hall electrode. By combining the self-aligned fabrication technique with the Ta-B electrode, a small value of critical switching current ($I_c \approx 79~\mu$A) is achieved despite a large MTJ size ($60 \times 150~\text{nm}^2$). We successfully reduce the write current to $48~\mu$A, utilizing a voltage-controlled magnetic anisotropy by applying the voltage to a MTJ: $V_{\text{MTJ}} = -1~$V. Moreover, the device also exhibits a low write error rate ($< 1 \times 10^{-8}$), high endurance ($> 1 \times 10^{12}$ cycles), and large break-down voltage ($> 2.5~$V). These results indicate that VoCSM with the Ta-B spin Hall electrode could open a path to realizing high-density nonvolatile memories with low power consumption and high-speed read and write operations.

I. INTRODUCTION

Spin-transfer-torque (STT) magnetic random-access memory (MRAM) has been intensively developed as a technology for nonvolatile memory with low power consumption and high-speed read and write operations [1–12]. However, STT write operations require some amount of write charge in order to switch the storage layer of magnetic tunnel junctions (MTJs), and such write operations consume much of the energy used during active operation. Moreover, as the MTJ size is reduced to realize a high-density STT MRAM, issues such as read disturbance and breakdown of the tunnel barrier in MTJs can arise. These issues emerge from the architecture of STT MRAM, where the same current path is used for both read and write operations, which means that there is an intrinsic physical limit to the miniaturization of STT MRAM. Recently, another write method that utilizes spin-orbit torque (SOT) originating from the spin Hall effect (SHE) with a three-terminal architecture called SOT MRAM has been proposed [13–24]. This write method can overcome these issues because it uses distinct current paths for read and write operations.

However, the write method results in a much larger cell size per bit for SOT MRAM compared with STT MRAM because SOT MRAM requires a three-terminal architecture. To overcome this, we propose a voltage-controlled spintronic memory (VoCSM). The VoCSM consists of a string of MTJs on the same spin Hall electrode, and utilizes voltage-controlled magnetic anisotropy (VCMA) for the selection of the MTJ and SHE for the write operation [25,26]. Although the VoCSM could offer smaller cell sizes per bit in principle, further improvements in write efficiency are required for scaled devices.

Materials as well as MTJ–spin-Hall-electrode interfaces with larger spin-orbit coupling have been attracting interest because they allow a larger amount of spin current (J_s) to be generated for manipulating the magnetic moments of the storage layer in the MTJs when the write current (J_e) is passed through the spin Hall electrode. Magnitudes of the spin Hall angle ($\theta_{\text{SH}} = J_s/J_e$) have been determined for various heavy transition metals by measuring the spin Hall magnetoresistance (SMR) and spin torque ferromagnetic resonance (ST FMR) [27–30] and by other means. Ta and W, in which the crystalline structure is polycrystalline *A*15 (β phase) or a mixture of β phase and amorphous phase, have large magnitudes of θ_{SH}. Recently, large magnitudes of θ_{SH} have also been observed in transition metal compounds such as W oxides and Cu oxides [31,32].

---

*Corresponding author. yushi.kato@toshiba.co.jp
†Present address: Center for Innovative Integrated Electronic Systems, Tohoku University, Sendai 980-8845, Japan.

In particular, W oxides have a larger magnitude of θ_{SH} (approximately -0.5) than W, which is expected to reduce the power consumption of the write operation for SOT MRAM. Unfortunately, these oxides are not compatible with the Co-Fe-B storage layer of MTJs in SOT MRAM because of a thick magnetic dead layer (DL) and a rough interface between the oxides and Co-Fe-B. In general, the ability to control a clear interface between the storage layer and the spin Hall electrode without dispersion of the structure and doping of impurities in the spin Hall electrode can be important for reducing the power consumption of write operations in SOT MRAM.

In this study, we investigate a Ta-B spin Hall electrode that is compatible with the Co-Fe-B storage layer of SOT MRAM. Moreover, we apply a self-aligned (SA) fabrication process [33] to prepare the VoCSM structures with amorphous Ta-B/Ta spin Hall electrode. We report a significant reduction in the write current by the combination of the new SHE material and the SA technique.

II. EXPERIMENT

We fabricate VoCSMs consisting of a string of eight MTJs on β-Ta or amorphous Ta-B/Ta spin Hall electrodes as shown in Fig. 1. Figure 1(a) shows a schematic diagram of the self-aligned VoCSM structure. Write current, which induces the SHE, is passed through the spin Hall electrode in the x direction. A voltage V_{MTJ} is applied across the MTJ, as shown in Fig. 1(a), to control the switching barrier height of the MTJs by the VCMA effect. The direction of magnetization of the MTJs is along the y axis, which is orthogonal to the write current. The MTJ structure on the spin Hall electrode is, from the top surface, Ta(5 nm)/Ir-Mn(8 nm)/Co-Fe(1.7 nm)/Ru(0.9 nm)/Co-Fe-B(1.8 nm)/MgO(1.6 nm)/Fe-B(2.2 nm) or Co-Fe-B (1.4 nm). The stacks are sputter-deposited on thermally oxidized Si wafers and annealed at 300 °C for 1 h in a magnetic field of 1 T. A magnetic field is applied during annealing in the in-plane direction to pin the magnetization of Co-Fe. The nominal compositions of Co-Fe-B and Fe-B are $Co_{40}Fe_{40}B_{20}$ and $Fe_{80}B_{20}$, respectively. A sintered $Ta_{50}B_{50}$ target is used for the deposition of the Ta-B spin

Hall electrode. Magnetization measurements are carried out without an applied voltage using a vibrational sample magnetometer (VSM) and the magneto-optical Kerr effect.

Scanning-electron-microscopy images of the VoCSM with the MTJ string delineated by a conventional fabrication method and an SA fabrication method are shown in Figs. 1(b) and 1(c), respectively. In the conventional method, the whole MTJ stack is patterned by electron-beam (EB) lithography followed by Ar-ion-beam etching (IBE), and then the electrode is patterned by photolithography and IBE. In the SA process, the MTJ stack perpendicular to the electrode is patterned first, and then the MTJ stack and the electrode are patterned simultaneously by EB lithography followed by IBE. As a result, the width of the MTJ and that of the spin Hall electrode are the same in the SA fabrication process, and almost all of the spin-polarized electrons can exert torque on the free layer. This allows us to greatly reduce the power consumption of the VoCSM with the SA spin Hall electrode. The size of the MTJs ($W \times L$) is changed from 30×90 nm^2 to 80×240 nm^2. The magnetoresistance ratios are 140% and 170% for the Ta-B and Ta spin Hall electrodes, respectively, and the resistance-area (RA) products and VCMA coefficients are 1 kΩ μm^2 and about 90 fJ/V m, respectively, for the MTJ on both electrodes.

The ST FMR devices are patterned using photolithography. The length and width of the devices are 100 and 20 μm, respectively. The resonance frequency is varied from 7 to 12 GHz.

The SMR devices are also patterned using photolithography. The width of the devices is 20 μm and the distance between voltage probes that measure the longitudinal resistance (R_{XX}) is 100 μm. External magnetic fields of up to 6 T are applied along the x, y and z axes in Fig. 6(a).

III. RESULTS AND DISCUSSION

A. Structural analysis and magnetic properties

Figure 2 shows (a) a cross-sectional high-resolution transmission-electron-microscopy (TEM) image of the MTJ, together with the fast-Fourier-transform (FFT) patterns of the (b) Ta, (c) Ta-B, (d) Fe-B, and (e) MgO layers.
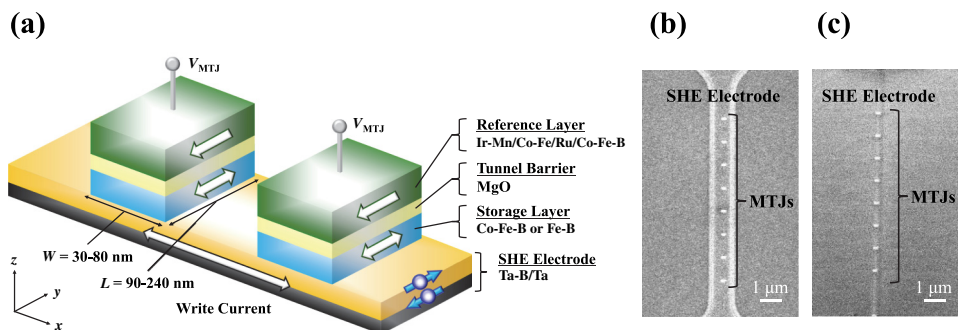
(a)

(b)   **(c)**

FIG. 1. (a) Schematic diagram of the self-aligned VoCSM structure with a Ta-B/Ta spin Hall electrode. The width of the spin Hall electrode is equal to the long-axis width of the MTJ in the self-aligned VoCSM structure. Scanning-electron-microscopy images of the VoCSM with a MTJ string on a (b) conventional spin Hall electrode and (c) self-aligned spin Hall electrode.
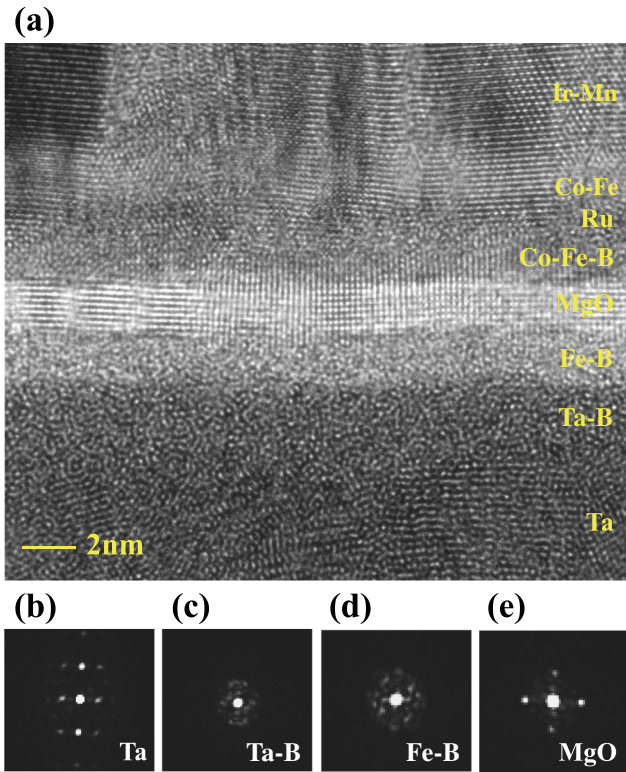
FIG. 2. (a) Cross-sectional high-resolution transmission-electron-microscopy image of the MTJ, and Fourier-transform patterns of the (b) Ta, (c) Ta-B, (d) Fe-B, and (e) MgO layers.

The FFT pattern of the Ta layer reveals a polycrystalline tetragonal β-Ta lattice structure. The Ta-B layer has an amorphous structure originating from its high B content.

The FFT pattern also shows that the Fe-B layer has an amorphous structure, and a sharp Fe-B/Ta-B interface is observed in the high-resolution TEM images. The MgO barrier layer has fine crystallinity and flatness along the (001) orientation.

Next, we examine the influence of the Ta-B insertion layer on magnetic properties such as DL, saturation magnetization (M_S), and perpendicular magnetic anisotropy. Magnetization are plotted as a function of Fe-B or Co-Fe-B thickness in the range of 1–3 nm. The plots show excellent linearity, allowing accurate estimation of the DL and M_S values of the Fe-B and Co-Fe-B layers. In Figs. 3(a) and 3(b), respectively, DL and M_S of the Fe-B layer and the Co-Fe-B layer are shown as a function of Ta-B thickness in the Ta-B/Ta bilayers. In Figs. 3(c) and 3(d), the effective magnetic anisotropy ($H_{k_{eff}}$) of the Fe-B layer and the Co-Fe-B layer is plotted against the storage-layer thickness for the Ta(3 nm)/MgO(1.6 nm)/Fe-B(t_{Fe-B} nm) and Co-Fe-B($t_{Co-Fe-B}$ nm)/Ta-B(t_{Ta-B})/Ta(10 nm) films, respectively. For both the Fe-B layer and Co-Fe-B layer, DL is estimated to be nearly zero for the films with Ta-B thickness from 1 to 5 nm in the Ta-B/Ta bilayers, as shown in Fig. 3(a). A sufficient decrease in DL is obtained only when the Ta-B layer thickness is larger than 1 nm. Thus, we successfully prepare an extremely small DL ferromagnetic layer with small interface roughness by using an amorphous boride spin Hall electrode. This indicates that the Ta-B underlayer is compatible with storage layers such as Fe-B and Co-Fe-B because the same boride compounds are used in the spin Hall electrode and ferromagnetic layer. As shown in Fig. 3(b), the estimated M_S is approximately 1250 emu/cm^3 for Fe-B and 1175 emu/cm^3 for Co-Fe-B
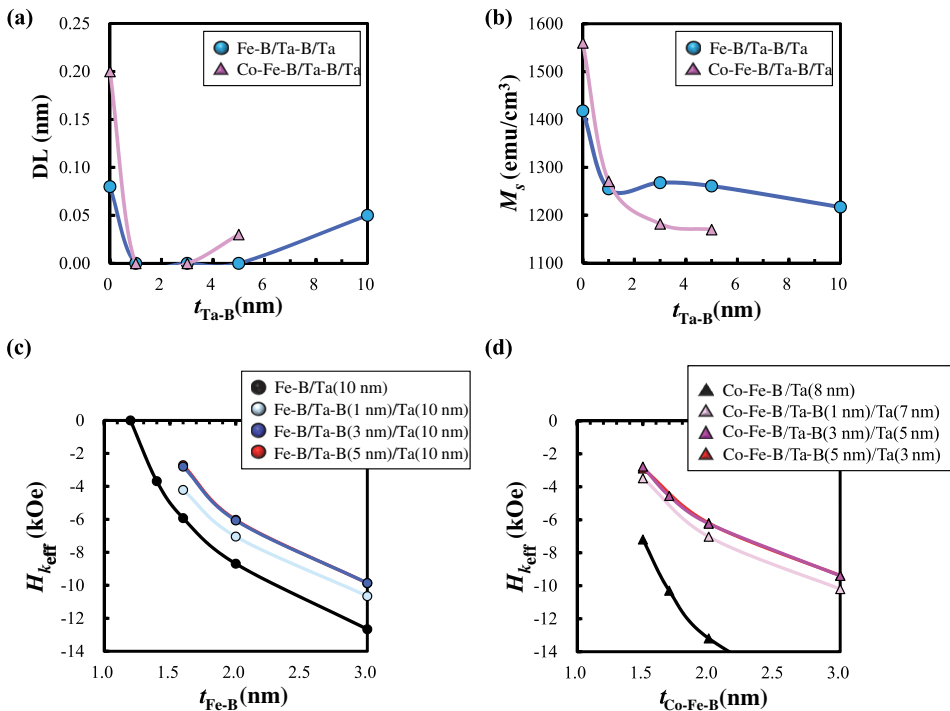

FIG. 3. (a) DL and (b) M_S of the Fe-B layer and the Co-Fe-B layer as a function of Ta-B thickness in Ta-B/Ta bilayers. $H_{k_{eff}}$ of (c) the Fe-B layer and (d) the Co-Fe-B layer plotted against the storage-layer thickness for various Ta-B thicknesses in the Ta-B/Ta bilayers.

on the Ta-B/Ta bilayers, which is lower than that of the Ta spin Hall electrode ($M_S \approx 1420$ emu/cm^3 for Fe-B and ≈ 1560 emu/cm^3 for Co-Fe-B). As in the case of DL, the Ta-B thickness of 1 nm sufficiently decreases M_S. The lower M_S is mainly caused by the suppression of B diffusion from the storage layer to the boride spin Hall electrode because the B concentration is much larger in Ta-B than in the storage layer. The magnitudes of negative $H_{k_{\text{eff}}}$ values shown in Figs. 3(c) and 3(d) indicate the existence of in-plane magnetic anisotropy in the storage layer. At the same storage-layer thickness of Fe-B and Co-Fe-B, the measured $H_{k_{\text{eff}}}$ values increase with increasing Ta-B thickness up to 3 nm and then became saturated for >3 nm. Within the experimental error, the $H_{k_{\text{eff}}}$ values for films with 3-nm-thick Ta-B are the same as the films with 5-nm-thick Ta-B, as shown in Figs. 3(c) and 3(d). The reason for the increase in $H_{k_{\text{eff}}}$ for Ta-B compared with Ta is the decrease in the demagnetizing field due to the small M_S values of the storage layer as shown in Fig. 3(b) and the decrease in DL for the storage layer/Ta-B as shown in Fig. 3(a). The estimated interface perpendicular magnetic anisotropy K_S at $V_{\text{MTJ}} = 0$ V is 1.90 erg/cm^2 for Co-Fe-B/Ta, 1.43 erg/cm^2 for Fe-B/Ta-B, and 1.16 erg/cm^2 for Co-Fe-B/Ta-B.

The VoCSM in this study employed in-plane MTJs. The critical switching current I_c in the present VoCSM is expressed as

$$I_{c0} \sim \frac{2e}{\hbar} \alpha M_S t_{\text{eff}} \left(\frac{H_{k_{\text{shape}}} + H_{k_{\text{ind}}}}{2} - \frac{H_{k_{\text{eff}}} - H_{k_{\text{eff}}}(V)}{2} \right)$$
$$\times \frac{w_N t_N}{\theta_{\text{SH}}}, \tag{1}$$

where e is the charge of an electron, α is a damping constant, $\hbar$ is Planck's constant divided by 2π, M_S is the saturation magnetization, t_{eff} is the effective thickness of the ferromagnetic layer, $H_{k_{\text{shape}}}$ is the in-plane shape magnetic anisotropy field, $H_{k_{\text{ind}}}$ is the in-plane induced magnetic anisotropy field, $H_{k_{\text{eff}}}$ is the effective perpendicular magnetic anisotropy field, $H_{k_{\text{eff}(V)}}$ is the variation of $H_{k_{\text{eff}}}$ by the applied voltage (V_{MTJ}), w_N and t_N are respectively the width and thickness of the SHE electrode, and θ_{SH} is the spin Hall angle. Since the VoCSM in this study employed in-plane MTJs, the energy variation depends on the magnetization direction within the horizontal plane, as expressed in Eq. (1). The effective in-plane magnetic anisotropy field can be separated by the shape and induced magnetic anisotropy fields. Figures 4(a) and 4(b) show the hysteresis loops measured by VSM and by applying in-plane magnetic fields along the easy and hard axes of the Co-Fe-B layer on Ta layer and Ta-B/Ta bilayers,

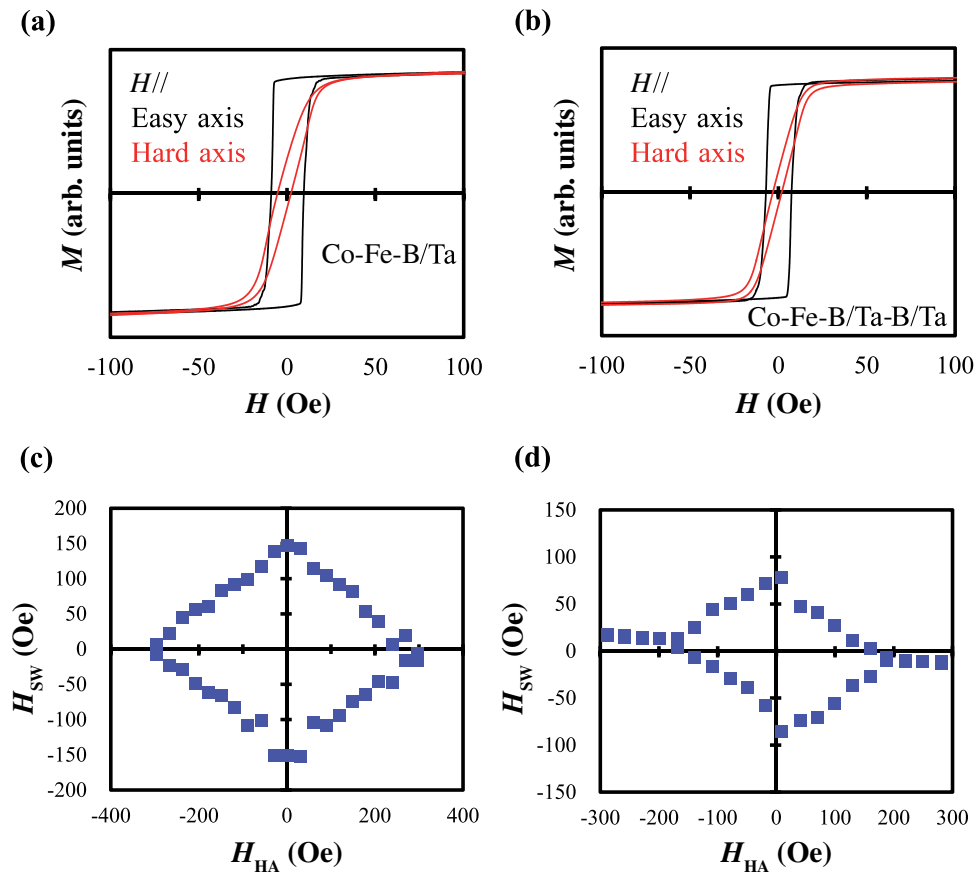**(a)**

(b)

(c)

(d)

FIG. 4. Hysteresis loops when in-plane magnetic field is applied along the easy and hard axes of the Co-Fe-B layer on (a) the Ta layer and (b) Ta-B/Ta bilayers. The typical asteroid curves of the Fe-B storage layer on Ta-B/Ta bilayers for the MTJ (60×180 nm^2) with (c) the conventional and (d) the self-aligned spin Hall electrode structure.

respectively. The in-plane induced magnetic anisotropy field $H_{k_{\text{ind}}}$ is estimated to have a value of approximately 40 Oe for Co-Fe-B(1.25 nm)/Ta(5 nm) and approximately 25 Oe for Co-Fe-B(1.5 nm)/Ta-B(3 nm)/Ta(5 nm), as shown in Figs. 4(a) and 4(b). Figures 4(c) and 4(d) represent the typical asteroid curve of the Fe-B storage layer on Ta-B/Ta bilayers for the MTJ (60×180 nm^2) with the conventional and the self-aligned structures, respectively. In Figs. 4(c) and 4(d), the magnetic field for switching is applied to the easy axis (y axis) and the magnetic field is applied to the hard axis (x axis) shown in Fig. 1(a). The in-plane shape magnetic anisotropy field $H_{k_{\text{shape}}}$ is estimated by the asteroid curve of the storage layer shown in Figs. 4(c) and 4(d). The $H_{k_{\text{shape}}}$ is induced by the aspect ratio of the MTJ, and has a value of approximately 300 Oe for the conventional structure and approximately 200 Oe for the self-aligned structure. This difference in the $H_{k_{\text{shape}}}$ is thought to be caused by the strain between the spin Hall electrode and the MTJ.

The effective perpendicular magnetic anisotropy field $H_{k_{\text{eff}}}$ is much larger than the effective in-plane magnetic anisotropy field ($H_{k_{\text{shape}}}$ and $H_{k_{\text{ind}}}$) and has an absolute value of -2.6 kOe for Co-Fe-B (1.25 nm)/Ta (5 nm) and -3.6 kOe for Co-Fe-B(1.5 nm)/Ta-B (3 nm)/Ta(5 nm), as described in Fig. 3(d). Consequently, the out-of-plane magnetization switching energy is dominant in this study, and thus Eq. (1) can be modified for the VoCSM as follows:

$$I_{c0} \sim \frac{2e}{\hbar} \alpha M_S t_{\text{eff}} \left(-\frac{H_{k_{\text{eff}}} - H_{k_{\text{eff}}(V)}}{2} \right) \frac{w_N t_N}{\theta_{\text{SH}}}. \quad (2)$$

In the precessional switching mode for in-plane MTJs, the spins in the storage layer precess from in-plane to out-of-plane, and thus increasing $H_{k_{\text{eff}}}$ has a big impact on lowering $\Delta_{\text{switching}}$, even though the total magnetization $M_S t_{\text{eff}}$ and the $H_{k_{\text{eff}}}$ are correlated significantly with the magnetic design in the device. In particular, lowering the total magnetization $M_S t_{\text{eff}}$ offers the advantage of lowering I_c, although it could also cause decreased retention Δ.

In this study, we are able to maintain the retention Δ by increasing t_{eff} (i.e., reducing DL) despite the decreased M_S. Consequently, from the perspective of lowering I_c, factors such as high θ_{SH}, self-aligned device structure related to small $w_N t_N$, high $H_{k_{\text{eff}}}$, low α, and low M_S all make similar contributions. Notably, the self-aligned device structure related to $w_N t_N$ and the spin Hall angle θ_{SH} are important factors, because they are independently controllable in the device.

We estimate the effective damping constant (α_{eff}) of the Co-Fe-B layer on Ta-B and Ta by using ST FMR. In the ST FMR measurement, Ta or Ta-B(2–12 nm)/Co-Fe-B(4 nm) bilayers are deposited on thermally oxidized Si wafers and annealed at 300 °C. To estimate the effective damping constant, we apply the following equation at zero dc-bias current [34]:

$$\Delta = \frac{2\pi f \, \alpha_{\text{eff}}}{\gamma}, \quad (3)$$

where Δ is the FMR measured linewidth, f is the resonance frequency, and γ is the gyromagnetic ratio. Figure 5 shows the effective damping constant (α_{eff}) of the Co-Fe-B layer estimated by ST FMR plotted against the Ta(t_{Ta}) and Ta-B($t_{\text{Ta-B}}$) thicknesses in the Co-Fe-B/Ta and Co-Fe-B/Ta-B bilayers, respectively. Circles indicate the experimental data including error bars and lines indicate the average value. The oxidized Ta or Ta-B layer thickness is subtracted in all calculations. The oxidized Ta or Ta-B layer thicknesses are estimated by cross-sectional TEM images (not shown here). In the region of t_{Ta}, $t_{\text{Ta-B}} > 2$ nm, the values of α_{eff} are nearly constant and estimated values of the α_{eff} of the Co-Fe-B layer in Co-Fe-B/Ta-B and Co-Fe-B/Ta from the t_{Ta}, $t_{\text{Ta-B}} > 2$ nm region are 0.0076 and 0.0073, respectively. For the Co-Fe-B/Ta case, the effective damping constant of the Co-Fe-B layer is almost consistent with the previous study [9]. For the precessional switching mode for in-plane MTJs, such as the VoCSM in the present study, a small value of α is required to achieve low switching current (I_c). We can achieve small values of
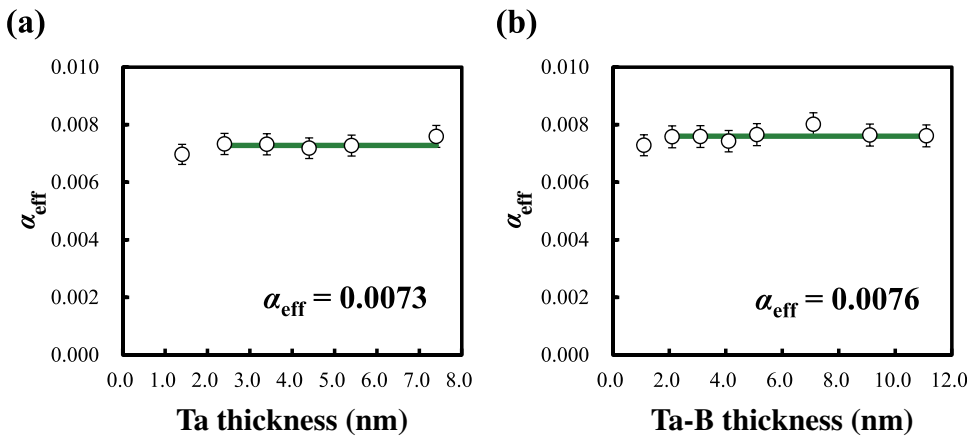
(a)

$$\alpha_{\text{eff}} = 0.0073$$

Ta thickness (nm)

(b)

$$\alpha_{\text{eff}} = 0.0076$$

Ta-B thickness (nm)

FIG. 5. Effective damping constant (α_{eff}) of the Co-Fe-B layer estimated by ST FMR plotted against (a) the Ta thickness in the Co-Fe-B/Ta bilayers and (b) the Ta-B thickness in the Co-Fe-B/Ta-B bilayers. Circles indicate the experimental data including error bars and lines indicate the average value in the region of t_{Ta}, $t_{\text{Ta-B}} > 2$ nm.

TABLE I.   Magnitude of the spin Hall angle ($|\theta_{SH}|$), the spin diffusion length (λ), and the resistivity (ρ) of the SHE electrodes estimated by the SMR fitting model of Refs. [27,35].

	Anneal temperature (°C)	Structure	$|\theta_{SH}|$	λ (nm)	ρ ($\mu\Omega$ cm)	Fitting model
Ta	300	β	0.09	0.64	157	Ref. [27]
Ta	400	β	0.07	0.55	164	Ref. [27]
Ta-B	300	Amorphous	0.18	1.02	197	Ref. [27]
Ta-B	400	Amorphous	0.17	0.97	186	Ref. [27]
Ta-B	300	Amorphous	0.20	1.02	197	Ref. [35]

α for both the Ta and Ta-B layers. From these results, we expect that the difference of the critical switching current I_c between the devices with Ta-B and Ta would be small from the perspective of the damping constant.

B. Spin Hall effect

We evaluate the spin-Hall-electrode properties, such as θ_{SH}, resistivity ρ, and spin diffusion length λ in the spin Hall electrode for Ta(1 nm)/MgO(1.6 nm)/Co-Fe-B (1.2 nm)/Ta(t_{Ta} nm) and Ta(1 nm)/MgO(1.6 nm)/Co-Fe-B (1.5 nm)/Ta-B(t_{Ta-B} nm) films by using SMR (Table I). Figure 6(a) shows a schematic diagram of the device used in SMR measurements and Fig. 6(b) shows SMR results [the definition is shown in Eq. (4)] as functions of the Ta and Ta-B SHE electrode thicknesses. The circles and triangles show the results for SMR devices annealed at 300°C and 400 °C, respectively. The solid and dashed curves are the result of fitting the measured data to the following equations [27]:

$$\text{SMR} = \frac{\Delta R_{XX}}{R_{XX}^Z} \sim \theta_{SH}^2 \frac{\lambda}{t_{SHE}} \frac{\tanh(t_{SHE}/2\lambda)}{1+\xi}$$
$$\times \left[1 - \frac{1}{\cosh(t_{SHE}/\lambda)} \right], \quad (4)$$

$$\xi \equiv \frac{\rho_{SHE} t_{FM}}{\rho_{FM} t_{SHE}}, \quad (5)$$

where t_{SHE} and t_{FM} are the thicknesses of the spin Hall electrode and ferromagnetic layer of Co-Fe-B, and ρ_{SHE} and ρ_{FM} are the resistivities of the spin Hall electrode and ferromagnetic layer of Co-Fe-B, respectively. The magnitudes of θ_{SH} and λ of the SHE electrodes are successfully obtained. The applied SMR model is based on the drift diffusion model [36], so that the estimated spin Hall angle and the spin diffusion length are all effective values. In the case of the devices annealed at 300 °C, the magnitudes of θ_{SH} evaluated by SMR are 0.09 and 0.18 for β-Ta and Ta-B, respectively. The signs are negative for β-Ta and Ta-B, and therefore $\theta_{SH} = -0.09$ and -0.18 for β-Ta and Ta-B, respectively. Thus, we observe a large magnitude of θ_{SH} for the amorphous Ta-B spin Hall electrode. A previous study of the Ta spin Hall electrode also suggested a large θ_{SH} (approximately -0.10) in the amorphouslike phase [27]. The crystal structure of commonly used heavy metals such as Ta depends on their thickness. Therefore, an amorphouslike structure is obtained in the thinner spin-Hall-electrode regions in Ref. [27]. However, our approach to creating an amorphous structure by using boride for heavy metals enables designs for a wider range of thicknesses. The resistivity and λ value of β-Ta are 157 $\mu\Omega$ cm and 0.64 nm, and those of Ta-B are 197 $\mu\Omega$ cm and 1.02 nm, respectively.

The magnitude of θ_{SH} is defined as $|\theta_{SH}| = |J_S/J_e|$, where J_e is the charge current density and $(\hbar/2e)J_S$ is the spin current density arising from the SHE [13]. Although
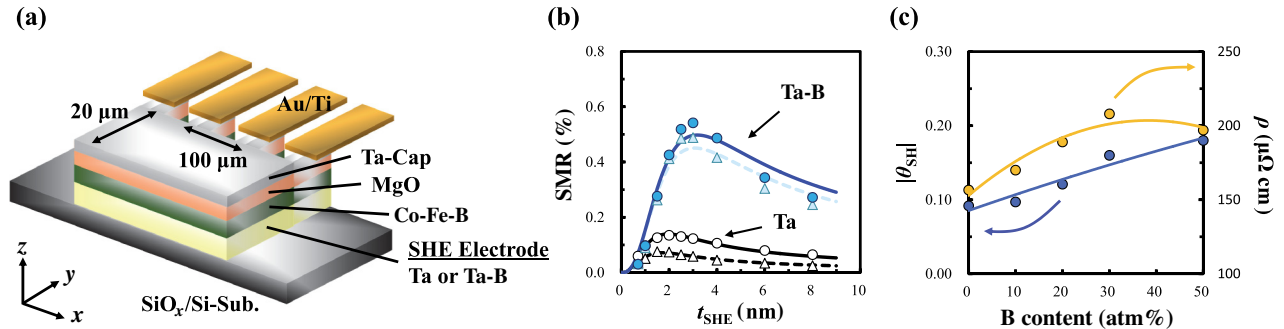

FIG. 6.   (a) Schematic diagram of the device used in SMR measurements. (b) Spin Hall magnetoresistance plotted against Ta and Ta-B thicknesses. Circles and triangles indicate the experimental data for devices annealed at 300 and 400 °C, respectively. Solid and dashed curves indicate results fitted to Eq. (2). (c) $|\theta_{SH}|$ and ρ estimated by SMR as a function of B content in the Ta$_{1-x}$B$_x$ spin Hall electrode. Solid lines in (c) are guides for the eyes.

the exact origins of the SHE are not fully understood, the magnitude of θ_{SH} is currently believed to arise from a combination of intrinsic mechanisms (spin-orbit interactions) and extrinsic effects (side jump [37] and skew scattering [38]) due to impurities. For the SHE in Ta-B, intrinsic mechanisms due to spin-orbit scattering originating from the $5d$ orbitals of Ta are expected to contribute to the large magnitude of θ_{SH}. However, since the intrinsic mechanism is governed by the electronic structures, it is difficult to discuss the role of the intrinsic effect in amorphous structures such as Ta-B. The exact origins of the SHE for Ta-B are not only the intrinsic mechanism but also extrinsic effects, which are based on the spin-orbit interaction. Basically, the larger spin Hall angle and longer spin diffusion length appear to be inconsistent with each other in the intrinsic mechanism [30]. Therefore, extrinsic effects might have a dominant role in the enhancement of the SHE of Ta-B. Because an increase in the resistivity from 157 to 197 $\mu\Omega$ cm is observed with increasing B content in Ta-B, as shown in Fig. 6(c), extrinsic effects such as side jump and skew scattering by B impurities are also expected to be mechanisms for the large magnitude of θ_{SH} in Ta-B. Moreover, we find that λ_{Ta-B} is longer than λ_{Ta}, which could be attributed to the large amount of light B metal, which has weak spin-orbit coupling in Ta-B. The value of λ_{Ta-B} linearly increases with B content up to $Ta_{50}B_{50}$, and the magnitude of θ_{SH} in Ta-B also increases with increasing B content up to $Ta_{50}B_{50}$, as shown in Fig. 6(c). From first-principles calculations [39,40], this kind of doped material exhibits a larger spin Hall angle and longer spin diffusion length, which are caused by skew scattering at substitutional impurities. This behavior seems to be similar to the trend for highly doped Ta-B. However, these theoretical results are obtained assuming the dilute limit on the number of impurities neglecting the intrinsic contribution. Further investigation is necessary to clarify the origins of the SHE for highly doped amorphous Ta-B.

The large magnitude of θ_{SH} in the Ta-B spin Hall electrode compared with the Ta spin Hall electrode is expected to reduce I_c as expressed in Eq. (1). For the devices annealed at 400 °C, the magnitude of θ_{SH} and λ_{Ta} of β-Ta are -0.07 and 0.55 nm, and those of Ta-B are -0.17 and 0.97 nm, respectively. In our experiment on sample preparation and SMR measurement, the level of uncertainty is mainly caused by variations in the Co-Fe-B and Ta-B (or β-Ta) thicknesses. The estimated experimental uncertainty is ±0.005 for the spin Hall angle and ±0.10 nm for the spin diffusion length, respectively. For both β-Ta and Ta-B, the magnitude of θ_{SH} and λ are almost constant for the devices annealed up to 400 °C within the experimental uncertainty. Thus, annealing tolerance is observed in the VoCSM with the Ta-B and β-Ta spin Hall electrodes up to 400 °C. The structural stabilities of the amorphous Ta-B and β-Ta spin

Hall electrodes are thought to be the origin of the annealing tolerance up to 400 °C.

In order to account for the roles of interfacial transparency and spin-mixing conductance, we apply another model from Ref. [35]. which is an extension of the equation in Ref. [27]. In the case of Ta-B annealed at 300 °C, the magnitude of θ_{SH} and the spin diffusion length evaluated by the model in Ref. [35] are -0.20 and 1.02 nm, respectively. The spin-mixing conductance $G_{mix\,eff}$ obtained by FMR is approximately 1.0×10^{19} m^{-2} for Co-Fe-B/Ta-B and approximately 1.3×10^{19} m^{-2} for Co-Fe-B/Ta. The estimated interfacial transparency T of Ta-B and β-Ta are about 0.60 and 0.50, respectively. The estimated interfacial transparency indicated that the spin loss layer at Co-Fe-B/Ta-B interface is lower than that at the Co-Fe-B/Ta interface. This is thought to be related to differences in the magnetic dead layer between the Co-Fe-B/Ta-B and Co-Fe-B/Ta interfaces. The intrinsic magnitude of θ_{SH} [41] estimated by θ_{SH}/T is 0.30 for Ta-B. The details of the FMR results are discussed elsewhere [42].

C. Device properties of the VoCSM

The switching properties are evaluated by applying a write current pulse to the spin Hall electrode and applying the V_{MTJ} to the reference layer of the MTJ, as shown in Fig. 1(a). No external field is applied to the device during measurement of switching properties. Other measurement conditions are described elsewhere [26]. Figure 7 shows the critical switching current density (J_{sw}) as a function of MTJ size for the conventional VoCSM structure with β-Ta and amorphous Ta-B/Ta spin Hall electrodes at $V_{MTJ} = 0$ V. The pulse width of the write current pulse is 50 ns. The J_{sw} values of the Ta-B/Ta bilayers are about half of those of β-Ta for all MTJ sizes. In both cases, J_{sw} approaches zero as the MTJ size decreases. This slope (dJ_{sw}/dW) represents the switching efficiency related to the difference in spin Hall angle. However, in the case
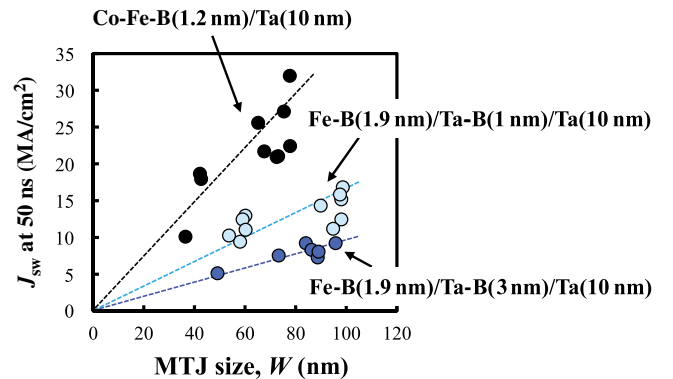

FIG. 7. J_{sw} versus MTJ size for the conventional VoCSM structure with β-Ta and Ta-B/Ta spin Hall electrodes at $V_{MTJ} = 0$ V. Dashed lines in Fig. 7 are guides for the eyes.

of MTJs smaller than about 40 nm, we will need to consider the magnetic domain of the storage layer on the Ta-B or Ta SHE electrode, because the switching mode in the storage layer will be changed from domain-wall motion to single-domain motion. Further investigation is needed to observe the magnetic domain of the storage layer on the Ta-B or Ta SHE electrode. The magnitudes of θ_{SH} of β-Ta and Ta-B are consistent with the J_{sw} values as shown in Fig. 7. However, as described above, the value of $\lambda_{Ta-B} = 1.02$ nm is larger than $\lambda_{Ta} = 0.64$ nm. When the values of J_{sw} are compared between VoCSMs with Fe-B/Ta-B(3 nm)/Ta(10 nm) and Fe-B/Ta-B(1 nm)/Ta(10 nm), the J_{sw} for Ta-B(3 nm) is smaller than for Ta-B(1 nm). This indicates that a thickness of 1 nm in Ta-B is not large enough to exert a large spin orbit torque on the Fe-B ferromagnetic layer due to the long spin diffusion length of Ta-B. The magnitude of the effective θ_{SH} values of β-Ta and Ta-B evaluated by using the J_{sw} values and Eq. (1) are 0.02 and 0.11, respectively. The magnitude of the effective θ_{SH} values are not consistent with those obtained by SMR. These differences might be related to the differences in DL and/or $M_S t_{eff}$ values between β-Ta and Ta-B. More effort is needed to understand the contributions to the switching current. The critical switching current density J_{sw} of the present VoCSM with the Co-Fe-B/Ta MTJs and the Fe-B/Ta-B (or Co-Fe-B/Ta-B) MTJs increases as the write current pulse is decreased. This indicates that magnetization reversal occurs by domain nucleation and propagation [19]. Moreover, the domain structure and Dzyaloshinskii-Moriya interaction are expected to be different between Co-Fe-B/Ta and Fe-B/Ta-B (or Co-Fe-B/Ta-B), which is will influence the nucleation and propagation dynamics [24]. Further investigation is needed to clarify the magnetization switching dynamics.

Figure 8(a) shows a typical resistance of MTJ versus write current when $V_{MTJ} = 0$ V, ± 1 V are applied and Fig. 8(b) shows a switching phase diagram plotted using the resistance versus write current curves, by using the Co-Fe-B storage layer, Ta-B spin Hall electrode, and SA fabrication process for the MTJ with a junction area of 60×150 nm². By combining the SA technique with

Ta-B, we obtain a small value of critical switching current ($I_c \approx 79$ μA) at $V_{MTJ} = 0$ V, even for the large MTJ size of 60×150 nm². Moreover, the write current is successfully reduced to 48 μA at $V_{MTJ} = -1$ V. As shown in Fig. 8(b), the bistable region expands as V_{MTJ} increases. Assuming that the main driving force for the change in the phase boundaries is the STT, the two phase boundaries are expected to move in parallel with increasing V_{MTJ}. Therefore, the behavior of the phase boundaries cannot be explained by STT only. The VCMA coefficient as estimated by the variation in $H_{k_{eff}}$ varies in the region of 80–100 fJ/V m, which is almost consistent with that reported in Ref. [26]. Therefore, the behavior of the V_{MTJ} dependence of the write current [the phase boundaries in Fig. 8(b)] is thought to be mainly affected by the VCMA effect.

Next, we discuss the influence on Joule heating during write current pulse flow. We roughly estimate the temperature during current injection. The Joule heating Q can be expressed as J^2/R (because $Q = V^2/R$, J is proportional to V). Therefore, the write current density J has a much larger influence on Joule heating than the resistance. The estimated device temperature reaches 100 °C when applying a constant current of ~ 2 mA ($\sim 5.5 \times 10^7$ A/cm²). On the other hand, when using Co-Fe-B/Ta-B, the write current is 50–100 μA [4–8 $\times 10^6$ A/cm²]. Because the write current density is one order smaller, the influence of Joule heating is thought to be two orders smaller in the case of Co-Fe-B/Ta-B compared with Co-Fe-B/Ta. Taking into account the use of a pulse current of 20 ns, the influence of Joule heating during the write operation would be negligibly small in Co-Fe-B/Ta-B MTJs.

Next, we discuss an influence on the Oersted magnetic field in more detail. In the case of the device shown in Fig. 7, both the Co-Fe-B/Ta MTJs and the Fe-B/Ta-B MTJs are fabricated using the conventional spin Hall electrode shown in Fig. 1(b). Hence, compared with these J_{sw}, the Oersted magnetic field is vanishingly small. In the case of Co-Fe-B/Ta-B MTJs prepared using the self-aligned spin Hall electrode shown in Fig. 1(c), the magnitude of the Oersted magnetic field $H \approx 4$ Oe, when using Ampere's
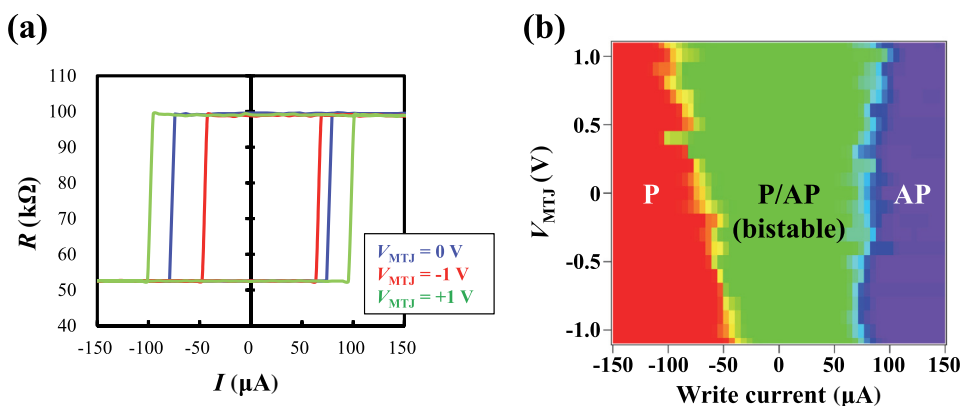

(a)

(b)

FIG. 8.   (a) Typical resistance of MTJ versus write current while $V_{MTJ} = 0$ V, ± 1 V is applied and (b) switching phase diagram plotted using the resistance versus write current curves, for the Co-Fe-B storage layer, Ta-B spin Hall electrode, and self-aligned fabrication process for MTJ with a junction area of 60×150 nm².
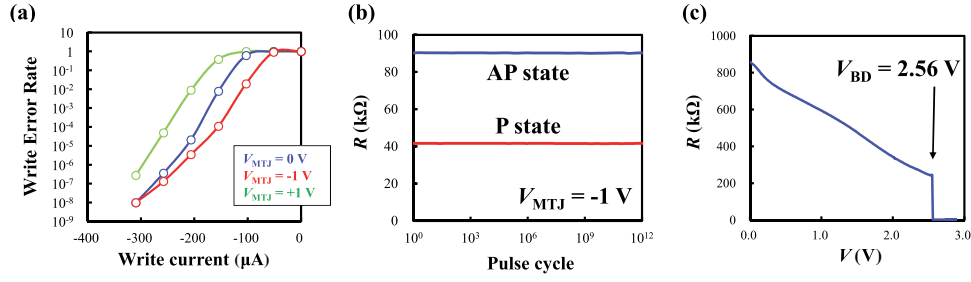
FIG. 9. (a) Write error rate as a function of write current while $V_{MTJ} = 0$ V, ± 1 V is applied, and (b) result of the endurance test of the MTJ at $V_{MTJ} = -1$ V when using a Co-Fe-B storage layer, Ta-B spin Hall electrode, and self-aligned fabrication process for the MTJ with a junction area of 60×150 nm^2. (c) Breakdown voltage (V_{BD}) for the MTJ (50×150 nm^2) with the conventional VoCSM structure and Ta-B(3 nm)/Ta(7 nm) bilayers.

rule and values of the write current $I = 100$ μA and with a perimeter of the SHE electrode of $l = 300$ nm. Thus, the Oersted magnetic field of the VoCSM with self-aligned structure is only 4 Oe, because the applied write current is quite small. Furthermore, the role of the Oersted magnetic field in the present VoCSM is different from the Co-Fe-B/Pt MTJs in Ref. [23]. In the present study, the Oersted magnetic field plays a role in disturbing the switching process, since both β-Ta and Ta-B have negative spin Hall angles.

We compare the I_c values between the present VoCSM, STT MRAM [43], and SOT MRAM [13,21,22]. It is noted that the benchmark of I_c is not always sufficient, because it is related to measurement conditions such as the write current pulse. In the present VoCSM, a value of I_c is achieved that is quite small despite a relatively large MTJ size compared with STT MRAM and SOT MRAM. First, the I_c values obtained for the VoCSM are quite small compared with SOT MRAM. This is because the present VoCSM is prepared by a self-aligned spin Hall electrode with a Ta-B, whereas the reference SOT MRAM is prepared using the conventional spin Hall electrode with a heavy metal (e.g., Ta, Pt). Second, almost the same values of I_c are obtained for the VoCSM compared with STT MRAM despite the relatively large MTJ size [43]. This suggests that, during spin Hall writing, one electron applies several spin torques to the magnetization of the storage layer along its distance of travel. It can be concluded that the combination of spin Hall writing with the VCMA effect, such as occurs in the present VoCSM, has a write efficiency that is about 4 times higher than STT writing [44].

For memory applications, a low write error rate (WER) and high breakdown voltage are important in MTJs for VoCSM. For the WER measurement at $V_{MTJ} = 0$ V, ± 1 V, we apply 10-μs cycles in the write process consisting of a 20-ns write current pulse and 9.98 μs waiting time. During the waiting time, the resistance of the MTJ is read. Figure 9(a) shows WER as a function of write current while $V_{MTJ} = 0$ V, ± 1 V are applied to the MTJ with a junction area of 60×150 nm^2 with a Co-Fe-B storage layer, Ta-B

spin Hall electrode, and SA fabrication process. When $V_{MTJ} = -1$ V is applied, the WER decreases with increasing write current and the WER curve is lower than for $V_{MTJ} = 0$ V. The measured WER for 20 ns write current pulses at $V_{MTJ} = 0$ V, -1 V is lower than 1.0×10^{-8}.

Finally, we present the results of endurance tests on the MTJ of the Ta-B spin Hall electrode in Fig. 9(b). For the endurance tests at $V_{MTJ} = -1$ V, we apply 50 ns cycles in the write process consisting of a 20 ns write current pulse and 30 ns waiting time. The magnitude of the write current employed is 517 μA. The MTJ exhibits no errors and no breakdown in 1×10^{12} cycles for the 20 ns write pulse at $V_{MTJ} = -1$ V even for the large applied write current of 517 μA. Figure 9(c) shows the breakdown voltage (V_{BD}) of the MTJ of the Ta-B spin Hall electrode. Because the thickness of the high-crystalline MgO barrier is 1.6 nm, the V_{BD} value is large ($V_{BD} > 2.5$ V). This is because we design the RA value to an order of 100–1000 Ω μm^2, since the voltage is applied to a selected MTJ in an operating VoCSM [25,26,33,43,44]. These results indicate that the proposed VoCSM with MTJs on the Ta-B spin Hall electrode can provide good performance with low WER, high endurance, and high V_{BD} for working memory.

IV. CONCLUSION

In summary, we investigate MTJs of a Ta-B spin Hall electrode for application in VoCSM. We successfully prepare an extremely small DL, lower M_S, and large $H_{k_{eff}}$ ferromagnetic layer with small interface roughness on an amorphous boride spin Hall electrode. The amorphous Ta-B spin Hall electrode has a large magnitude of θ_{SH} ($\theta_{SH} = -0.18$), and this approach using boride as the heavy metal enables designs using a wider range of Ta-B thicknesses and is compatible with the Co-Fe-B storage layer of MTJs in SOT MRAM. In this way, we successfully reduce the write current by using SOT. By combining the SA technique with Ta-B, we achieve a small value of critical switching current ($I_c \approx 79$ μA) even for large MTJ junction sizes (60×150 nm^2). We successfully reduce the write

current further to 48 μA at $V_{MTJ} = -1$ V. Moreover, the MTJ on the Ta-B spin Hall electrode is found to exhibit low WER ($<1.0 \times 10^{-8}$), high endurance ($>1 \times 10^{12}$ cycles), and large V_{BD} (>2.5 V). These results indicate that the VoCSM with MTJs on the Ta-B spin Hall electrode could open a path to realizing high-density nonvolatile memory with low power consumption and high-speed read and write operations.

ACKNOWLEDGMENTS

[1] J. C. Slonczewski, Current-driven excitation of magnetic multilayers, J. Magn. Magn. Mater. **159**, L1 (1996).

[2] J. A. Katine, F. J. Albert, R. A. Buhrman, E. B. Myers, and D. C. Ralph, Current-Driven Magnetization Reversal and Spin-Wave Excitations in Co/ Cu/ Co Pillars, Phys. Rev. Lett. **84**, 3149 (2000).

[3] T. Kishi, H. Yoda, T. Kai, T. Nagase, E. Kitagawa, M. Yoshikawa, K. Nishiyama, T. Daibou, M. Nagamine, M. Amano, S. Takahashi, M. Nakayama, N. Shimomura, H. Aikawa, S. Ikegawa, S. Yuasa, K. Yakushiji, H. Kubota, A. Fukushima, M. Oogane, T. Miyazaki, and K. Ando, in IEDM Technical Digest (2008), p. 309.

[4] S.-W. Chung, T. Kishi, J. W. Park, M. Yoshikawa, K. S. Park, T. Nagase, K. Sunouchi, H. Kanaya, G. C. Kim, K. Noma, M. S. Lee, A. Yamamoto, K. M. Rho, K. Tsuchida, S. J. Chung, J. Y. Yi, H. S. Kim, Y. S. Chun, H. Oyamatsu, and S. J. Hong, in IEDM Technical Digest (2016), p. 27.

[5] K. J. Lee, Y. Liu, A. Deac, M. Li, J. W. Chang, S. Liao, K. Ju, O. Redon, J. P. Nozières, and B. Dieny, Spin transfer effect in spin-valve pillars for current-perpendicular-to-plane magnetoresistive heads (invited), J. Appl. Phys. **95**, 7423 (2004).

[6] S. Ikeda, J. Hayakawa, Y. M. Lee, F. Matsukura, Y. Ohno, T. Hanyu, and H. Ohno, Magnetic tunnel junctions for spintronic memories and beyond, IEEE Trans. Electron Devices **54**, 991 (2007).

[7] Z. Diao, A. Panchula, Y. Ding, M. Pakala, S. Wang, Z. Li, D. Apalkov, H. Nagai, A. Driskill-Smith, L.-C. Wang, E. Chen, and Y. Huai, Spin transfer switching in dual MgO magnetic tunnel junctions, Appl. Phys. Lett. **90**, 132508 (2007).

[8] S. Mangin, D. Ravelosona, J. A. Katine, M. J. Carey, B. D. Terris, and E. E. Fullerton, Current-induced magnetization reversal in nanopillars with perpendicular anisotropy, Nat. Mater. **5**, 210 (2006).

[9] S. Ikeda, K. Miura, H. Yamamoto, K. Mizunuma, H. D. Gan, M. Endo, S. Kanai, J. Hayakawa, F. Matsukura, and H. Ohno, A perpendicular-anisotropy CoFeB-MgO magnetic tunnel junction, Nat. Mater. **9**, 721 (2010).

[10] S.-M. Seo and K.-J. Lee, Current-induced synchronized switching of magnetization, Appl. Phys. Lett. **101**, 062408 (2012).

[11] N. D. Rizzo, D. Houssameddine, J. Janesky, R. Whig, F. B. Mancoff, M. L. Schneider, M. DeHerrera, J. J. Sun, K. Nagel, S. Deshpande, H.-J. Chia, S. M. Alam, T. Andre, S. Aggarwal, and J. M. Slaughter, A fully functional 64 Mb DDR3 ST-MRAM built on 90 nm CMOS technology, IEEE Trans. Magn. **49**, 4441 (2013).

[12] H. Yoda, E. Kitagawa, N. Shimomura, S. Fujita, and M. Amano, in Symposia on VLSI Technology (2015), p. T104.

[13] L. Liu, C.-F. Pai, Y. Li, H. W. Tseng, D. C. Ralph, and R. A. Buhrman, Spin-torque switching with the giant spin Hall effect of tantalum, Science **336**, 555 (2012).

[14] A. Chernyshov, M. Overby, X. Liu, J. K. Furdyna, Y. Lyanda-Geller, and L. P. Rokhinson, Evidence for reversible control of magnetization in a ferromagnetic material by means of spin-orbit magnetic field, Nat. Phys. **5**, 656 (2009).

[15] I. M. Miron, K. Garello, G. Gaudin, P.-J. Zermatten, M. V. Costache, S. Auffret, S. Bandiera, B. Rodmacq, A. Schuhl, and P. Gambardella, Perpendicular switching of a single ferromagnetic layer induced by in-plane current injection, Nature **476**, 189 (2011).

[16] J. Kim, J. Sinha, M. Hayashi, M. Yamanouchi, S. Fukami, T. Suzuki, S. Mitani, and H. Ohno, Layer thickness dependence of the current-induced effective field vector in Ta/ CoFeB/ MgO, Nat. Mater. **12**, 240 (2013).

[17] S. Fukami, T. Anekawa, C. Zhang, and H. Ohno, A spin-orbit torque switching scheme with collinear magnetic easy axis and current configuration, Nat. Nanotechnol. **11**, 621 (2016).

[18] K.-S. Lee, S.-W. Lee, B.-C. Min, and K.-J. Lee, Thermally activated switching of perpendicular magnet by spin-orbit spin torque, Appl. Phys. Lett. **104**, 072413 (2014).

[19] K. Garello, C. O. Avci, I. M. Miron, M. Baumgartner, A. Ghosh, S. Auffret, O. Boulle, G. Gaudin, and P. Gambardella, Ultrafast magnetization switching by spin-orbit torques, Appl. Phys. Lett. **105**, 212402 (2014).

[20] C. Zhang, S. Fukami, H. Sato, F. Matsukura, and H. Ohno, Spin-orbit torque induced magnetization switching in nanoscale Ta/ CoFeB/ MgO, Appl. Phys. Lett. **107**, 012401 (2015).

[21] M.-H. Nguyen, C.-F. Pai, K. X. Nguyen, D. A. Muller, D. C. Ralph, and R. A. Buhrman, Enhancement of the anti-damping spin torque efficacy of platinum by interface modification, Appl. Phys. Lett. **106**, 222402 (2015).

[22] S. Fukami, T. Anekawa, C. Zhang, and H. Ohno, A spin-orbit torque switching scheme with collinear magnetic easy axis and current configuration, Nat. Nanotechnol. **10**, 1038 (2016).

[23] S. V. Aradhya, G. E. Rowlands, J. Oh, D. C. Ralph, and R. A. Buhrman, Nanosecond-timescale low energy switching of in-plane magnetic tunnel junctions through dynamic oersted-field-assisted spin Hall effect, Nano Lett. **16**, 5987 (2016).

[24] M. Baumgartner, K. Garello, J. Mendil, C. O. Avci, E. Grimaldi, C. Murer, J. Feng, M. Gabureac, C. Stamm, Y. Acremann, S. Finizio, S. Wintz, J. Raabe, and P. Gambardella, Spatially and time-resolved magnetization dynamics driven by spin-orbit torques, Nat. Nanotechnol. **12**, 980 (2017).

[25] H. Yoda, N. Shimomura, Y. Ohsawa, S. Shirotori, Y. Kato, T. Inokuchi, Y. Kamiguchi, B. Altansargai, Y. Saito, K.

Koi, H. Sugiyama, S. Oikawa, M. Shimizu, M. Ishikawa, K. Ikegami, and A. Kurobe, in IEDM Technical Digest (2016), p. 27-6.

[26] T. Inokuchi, H. Yoda, Y. Kato, M. Shimizu, S. Shirotori, N. Shimomura, K. Koi, Y. Kamiguchi, H. Sugiyama, S. Oikawa, K. Ikegami, M. Ishikawa, B. Altansargai, A. Tiwari, Y. Ohsawa, Y. Saito, and A. Kurobe, Improved read disturb and write error rates in voltage-control Spintronics memory (VoCSM) by controlling energy barrier height, Appl. Phys. Lett. **110,** 252404 (2017).

[27] J. Liu, T. Ohkubo, S. Mitani, K. Hono, and M. Hayashi, Correlation between the spin Hall angle and the structural phases of early 5d transition metals, Appl. Phys. Lett. **107,** 232408 (2015).

[28] C.-F. Pai, L. Liu, Y. Li, H. W. Tseng, D. C. Ralph, and R. A. Buhrman, Spin transfer torque devices utilizing the giant spin Hall effect of tungsten, Appl. Phys. Lett. **101,** 122404 (2012).

[29] A. Ganguly, K. Kondou, H. Sukegawa, S. Mitani, S. Kasai, Y. Niimi, Y. Otani, and A. Barman, Thickness dependence of spin torque ferromagnetic resonance in $Co_{75}Fe_{25}$/Pt bilayer films, Appl. Phys. Lett. **104,** 072405 (2014).

[30] Y. Wang, P. Deorani, X. Qiu, J. H. Kwon, and H. Yang, Determination of intrinsic spin Hall angle in Pt, Appl. Phys. Lett. **105,** 152412 (2014).

[31] H. An, Y. Kageyama, Y. Kanno, N. Enishi, and K. Ando, Spin-torque generator engineered by natural oxidation of Cu, Nat. Commun. **7,** 13069 (2016).

[32] K.-U. Demasius, T. Phung, W. Zhang, B. P. Hughes, S.-H. Yang, A. Kellock, W. Han, A. Pushp, and S. Parkin, Enhanced spin-orbit torques by oxygen incorporation in tungsten films, Nat. Commun. **7,** 10644 (2016).

[33] S. Shirotori, H. Yoda, Y. Ohsawa, N. Shimomura, T. Inokuchi, Y. Kato, Y. Kamiguchi, K. Koi, K. Ikegami, H. Sugiyama, M. Shimizu, B. Altansargai, S. Oikawa, M. Ishikawa, A. Tiwari, Y. Saito, and A. Kurobe, Voltage-control spintronics memory with a self-aligned heavy-metal electrode, IEEE Trans. Magnet. **53,** 3401104 (2017).

[34] L. Liu, T. Moriyama, D. C. Ralph, and R. A. Buhrman, Spin-Torque Ferromagnetic Resonance Induced by the Spin Hall Effect, Phys. Rev. Lett. **106,** 036601 (2011).

[35] J. Kim, P. Sheng, S. Takahashi, S. Mitani, and M. Hayashi, Spin Hall Magnetoresistance in Metallic Bilayers, Phys. Rev. Lett. **116,** 097201 (2016).

[36] V. P. Amin and M. D. Stiles, Spin transport at interfaces with spin-orbit coupling: Phenomenology, Phys. Rev. B **94,** 104420 (2016).

[37] L. Berger, Side-jump mechanism for the Hall effect of ferromagnets, Phys. Rev. B **2,** 4559 (1970).

[38] J. Smit, The spontaneous hall effect in ferromagnetics II, Physica **24,** 39 (1958).

[39] M. Gradhand, D. V. Fedorov, P. Zahn, and I. Mertig, Extrinsic Spin Hall Effect from First Principles, Phys. Rev. Lett. **104,** 186403 (2010).

[40] M. Gradhand, D. V. Fedorov, P. Zahn, and I. Mertig, Spin Hall angle versus spin diffusion length: Tailored by impurities, Phys. Rev. B **81,** 245109 (2010).

[41] W. Zhang, W. Han, X. Jiang, S.-H. Yang, and S. Parkin, Role of transparency of platinum-ferromagnet interfaces in determining the intrinsic magnitude of the spin Hall effect, Nat. Phys. **11,** 496 (2015).

[42] A. Tiwari, H. Yoda, Y. Kato, K. Koi, M. Ishikawa, S. Oikawa, Y. Saito, T. Inokuchi, N. Shimomura, M. Shimizu, S. Shirotori, B. Altansargai, H. Sugiyama, Y. Ohsawa, and A. Kurobe, in Digests of Intermag 2018, ED-07, Singapore, 26 Apr., 2018.

[43] Y. Ohsawa, H. Yoda, N. Shimomura, S. Shirotori, S. Fujita, K. Koi, B. Altansargai, S. Oikawa, M. Shimizu, Y. Kato, T. Inokuchi, H. Sugiyama, M. Ishikawa, T. Ajay, K. Ikegami, S. Takaya, and A. Kurobe, in Digests of EDTM 2018, 9A-01, Kobe, Japan, 16 Mar., 2018.

[44] H. Yoda, T. Inokuchi, M. Shimizu, Y. Kato, N. Shimomura, Y. Ohsawa, Y. Saito, S. Shirotori, S. Oikawa, K. Koi, B. Altansargai, H. Sugiyama, M. Ishikawa, Y. Kamiguchi, K. Ikegami, and A. Kurobe, in Proceedings of e-NVM 2017, Gardanne, France, 25-27 Sep., 2017.